



1 **Simulated Particle Evolution within a Winter Storm: Contributions of Riming to Radar**
2 **Moments and Precipitation Fallout**

3

4

5 *Andrew DeLaFrance¹, Lynn A. McMurdie¹, Angela K. Rowe², Andrew J. Heymsfield^{3,4}*

6

7

8 *¹Department of Atmospheric Sciences, University of Washington,*

9 *Seattle, WA, USA*

10 *²Department of Atmospheric and Oceanic Sciences, University of Wisconsin-Madison,*

11 *Madison, WI, USA*

12 *³National Center for Atmospheric Research,*

13 *Boulder, Co, USA*

14 *⁴U.S. National Science Foundation,*

15 *Alexandria, VA, USA*

16

17

18 *Correspondence to: Andrew DeLaFrance (adelaf@uw.edu)*

19

20

21

22

23

24

25

26

27

28

29

30

31



32

Abstract

33

Remote sensing radars from air- and spaceborne platforms provide critical observations of clouds

34

to estimate precipitation rates across the globe. Capability of these radars to detect changes in

35

precipitation properties is advanced by Doppler measurements of particle fall speed. Within

36

mixed-phase clouds, precipitation mass and its fall characteristics are especially sensitive to the

37

effects of riming. In this study, we quantified these effects and investigated the distinction of

38

riming from aggregation in Doppler radar vertical profiles using quasi-idealized particle-based

39

model simulations. Observational constraints of a control simulation were determined from

40

airborne in situ and remote sensing measurements collected during the Investigation of

41

Microphysics and Precipitation for Atlantic Coast-Threatening Snowstorms (IMPACTS) for a

42

wintery-mixed precipitation event over the northeast United States on 04 February 2022. From the

43

upper boundary of a one-dimensional column, particle evolution was simulated through vapor

44

deposition, aggregation, and riming processes, producing realistic Doppler radar profiles. Despite

45

a modest observed amount of supercooled liquid water (0.05 g m^{-3}), riming accounted for 55% of

46

the ice-phase precipitation mass, cumulatively increasing reflectivity by 6.1 dB and Doppler

47

velocity by 0.9 m s^{-1} . Independent evaluation of process-based sensitivities showed that while

48

radar reflectivity is comparably sensitive to either riming- or aggregation-based particle

49

morphology, the Doppler velocity profile is uniquely sensitive to particle density changes during

50

riming. Thus, Doppler velocity profiles advance the diagnosis of riming as a dominant

51

microphysical process in stratiform clouds from single-wavelength radars, which has

52

implications for quantitative constraints of particle properties in remote sensing applications.

53

54

55

56

57

58

59

60

61

62



63 1. Introduction

64 Ice crystals within precipitating winter storms evolve through an inherently stochastic
65 sequence of microphysical processes which uniquely affect their physical properties and fall
66 characteristics. This continuous and process-based evolution of ice-phase particles remains
67 poorly represented by many numerical models and remote sensing retrieval algorithms. A
68 fundamental limitation is that cloud and precipitation processes occur on physical scales that are
69 several orders of magnitude smaller than typical cloud-scale model grids or the remote sensing
70 instrument sampling volume. Nevertheless, realistic representation of varied particle populations
71 within clouds is necessary to accurately estimate precipitation rates.

72 Commonly, populations of particles within some volume are expressed by a particle size
73 distribution (PSD), and weighted integrals (i.e., moments) of the PSD are sensitive to the
74 microphysical evolution of ice-phase particles (Morrison et al. 2020). Ice-phase precipitation
75 mass is proportional to the second moment of the PSD. Because radar reflectivity, Z , is
76 proportional to the square of the mass (i.e., the fourth moment of the PSD), the precipitation
77 mass directly affects power returned to a radar. However, because of the physical complexity
78 arising from diversity in initial ice crystal habits and their unique process-based morphologies
79 with time, assumptions about the particle properties and the PSD are often necessary to derive
80 remote sensing precipitation rate estimates. For example, ice crystals are commonly assumed to
81 be spherical (e.g., Iguchi et al. 2018) and the population may be constrained to a prescriptive
82 PSD shape or snow density (e.g., Grecu et al. 2016). A consequence of such a priori assumptions
83 is that process-based variations cannot be expressed and retrieved precipitation rate estimates are
84 inherently constrained, leading to snowfall rate underestimation and increased error compared to
85 liquid phase (e.g., Speirs et al. 2017). To advance the utility of radar remote sensing
86 measurements of ice-phase precipitation, it is important to understand the quantitative effects of
87 process-based evolution on the intrinsic physical properties of precipitation in natural clouds and
88 their implications for the radar measurements.

89 A remarkable property of precipitating clouds is that liquid water droplets are frequently
90 present at sub-freezing temperatures alongside ice crystals. A region of cloud containing both ice
91 and sub-freezing (i.e., supercooled) liquid water (SLW) is described as a mixed-phase layer. One
92 implication of the mixed phase particle population is that depositional ice growth occurs at the
93 expense of liquid water due to differences in saturation vapor pressures over ice and liquid



94 surfaces, a process commonly referred to as the Wegener-Bergeron-Findeisen process
95 (Pruppacher and Klett 1997). Additionally, upon contact with falling ice crystals, the SLW
96 droplets freeze and are accreted by the crystal (i.e., riming), initiating a physical morphology of
97 the particle. Natural ice crystals demonstrate tremendous variability in shape and complexity
98 depending on growth habits (e.g., Magono and Lee 1966; Pruppacher and Klett 1997; Bailey and
99 Hallet 2009). Because of this diversity, it is often convenient to define the crystal size along
100 major and minor axes while the major axis is assumed to be along the maximum dimension of
101 the crystal and the minor axis is along an orthogonal orientation. The aspect ratio defines the
102 ratio between the crystal dimensions along the minor and major axes (Jensen and Harrington
103 2015). One commonly adopted conceptual description for the change in particle properties
104 during riming is the “fill-in” model (Heymsfield 1982) whereby the liquid water will initially fill
105 open voids, while largely maintaining the initial dimensions of the crystal axes. During later
106 stages of the “fill-in” riming model, rime accumulates on the underside of the falling crystal,
107 increasing the minor dimension of the crystal while the major dimension remains unchanged.
108 With increasing riming, aspect ratio approaches unity, which is expected for heavily rimed
109 graupel particles. Consequently, riming results in increasing particle density and, therefore, fall
110 velocity. The adjustments in particle geometry and fall characteristics with rime accumulation
111 are relative to, and dependent on, the initial ice crystal geometry and accreted rime but further
112 dependent on prior and concurrent processes including vapor depositional growth and
113 aggregation (e.g., Jensen and Harrington 2015).

114 Ice-phase particle growth by deposition of vapor-phase water directly increases the ice water
115 content (IWC) and therefore, yields direct increases in Z (Field et al. 2005, 2007). However,
116 depositional mass accumulation occurs at a relatively slow rate, thus, gradual increases in Z are
117 expected from depositional growth alone. Aggregation of two or more particles does not
118 explicitly alter the IWC of the particles, but rather redistributes the mass to a larger size particle.
119 Despite unchanging IWC, increased particle diameters, D , during aggregation enhances radar
120 scattering at a rate proportional to D^6 and consequently, Z may be significantly increased by
121 effects of aggregation. Through accumulation of liquid-phase water which yields increases in
122 IWC, similar, rapid adjustments in Z are also possible during riming. Evaluation of process-
123 based effects on the evolution of the PSD moments and their implications for precipitation
124 fallout from natural clouds is challenging because specific processes cannot be readily isolated,



125 even if observations are collected in situ. In general, observationally-consistent numerical
126 modeling simulations are necessary to determine such effects.

127 The physical scales of processes that govern the formation and evolution of falling ice
128 crystals are not resolved by most numerical models. In bulk- and bin-microphysics schemes, ice-
129 phase processes are commonly expressed implicitly through conversion processes whereby
130 precipitation is exchanged among predefined categories (e.g., ice, snow, graupel, hail; Thompson
131 et al. 2004; Morrison et al. 2005). However, prior studies (e.g., Colle et al. 2005; Morrison and
132 Milbrandt 2011; van Weverberg et al. 2012) have demonstrated that the precipitation evolution
133 and fallout is sensitive to a priori thresholds that define category conversions (e.g., snow to
134 graupel during riming). For rimed growth, Lagrangian particle-based model simulations indicate
135 that bulk particle density can undergo rapid evolution in response to small variations in the
136 background SLW concentration, significantly modulating the particle fall velocity and surface
137 precipitation rate (DeLaFrance et al. 2024). For remote sensing retrievals of mixed-phase
138 precipitation, the effects of rime accumulation are constrained by the a priori assumptions about
139 the particle's mass, geometry, or fall characteristics. Recently, diverse methodologies leveraging
140 multi-frequency, dual-polarization, and Doppler radar measurements have been proposed for
141 retrieving some properties of ice-phase particles that would otherwise be prescribed (e.g.,
142 Leinonen and Szyrmer 2015; Kneifel et al. 2016; Moisseev et al. 2017; Oue et al. 2018;
143 Leinonen et al. 2018; Mason et al. 2019, Chase et al. 2021). Among these methods, leveraging
144 radar Doppler data has shown promise in inferring the onset of riming and, subsequently, the
145 riming-based modulations of retrieved particle property estimates. Mason et al. (2018)
146 demonstrated that the addition of Doppler radar measurements provides constraint on the bulk
147 ice density parameter in retrievals of snowfall. Furthermore, as shown by Kalesse et al. (2016),
148 rimed snow occupies a unique region of Doppler spectra distinct from unrimed snow. One-
149 dimensional (1D) spectral bin microphysics modeling simulations have shown promise in
150 reproducing the Doppler spectra moments of riming but demonstrate sensitivity to particle
151 property assumptions (Kalesse et al. 2016).

152 The 1D columnar modeling approach offers a framework for simulating explicit
153 microphysical processes and detailed particle properties that are computationally prohibitive in a
154 three-dimensional (3D) dynamic model. The 1D construction is therefore well suited to advanced
155 bin and Lagrangian particle-based microphysics schemes. One challenge for such simulation



156 designs, however, is constraining the model in a way that minimizes assumptions and, as a result,
157 ambiguity in the attributing physical process for adjustments in the cloud's radar and
158 precipitation characteristics (e.g., Kalesse et al. 2016; Bringi et al. 2020). Some assumptions can
159 be constrained by coincident in situ and remote sensing radar measurements.

160 Data collected during winters of 2020, 2022, and 2023 from the Investigation of
161 Microphysics and Precipitation for Atlantic Coast Threatening Snowstorms (IMPACTS)
162 campaign (McMurdie et al. 2022) provide those constraints. Midlatitude cyclones over the
163 United States East Coast and Midwest regions were comprehensively sampled by coordinated
164 aircraft- and ground-based platforms to better understand the precipitation microphysics within
165 regions of snowfall that organize into elongated regions commonly recognized as snowbands
166 (e.g., Novak et al. 2004). Consistent with IMPACTS's goal to support improved numerical
167 modeling and remote sensing retrievals of winter precipitation, in the present study we
168 investigate the process-based effects of riming in a sampled storm that produced moderate rates
169 of wintry-mixed precipitation for a prolonged period over the Northeast. Our overarching
170 approach is to combine these observations with numerical modeling simulations to describe the
171 process-based particle evolution and contributions of riming to the observed radar properties and
172 precipitation rates. Here, we use an observationally-constrained, sophisticated Lagrangian
173 particle-based model within a 1D columnar framework to address the following questions:

- 174 1. Can primary ice processes (i.e., deposition, aggregation, riming) within a simplified
175 1D simulation reasonably reproduce the observed evolution of particles within the
176 natural cloud?
- 177 2. What were the quantitative contributions of riming to the observed Doppler radar
178 vertical profiles and to the surface precipitation rate?
- 179 3. Do simulated Doppler radar vertical profiles yield characteristic responses to the
180 onset or degree of riming that is distinct from other ice-phase processes (e.g.,
181 aggregation)?

182

183 **2. Winter Storm Observations**

184 **2.1. 04 February 2022 Case Study**

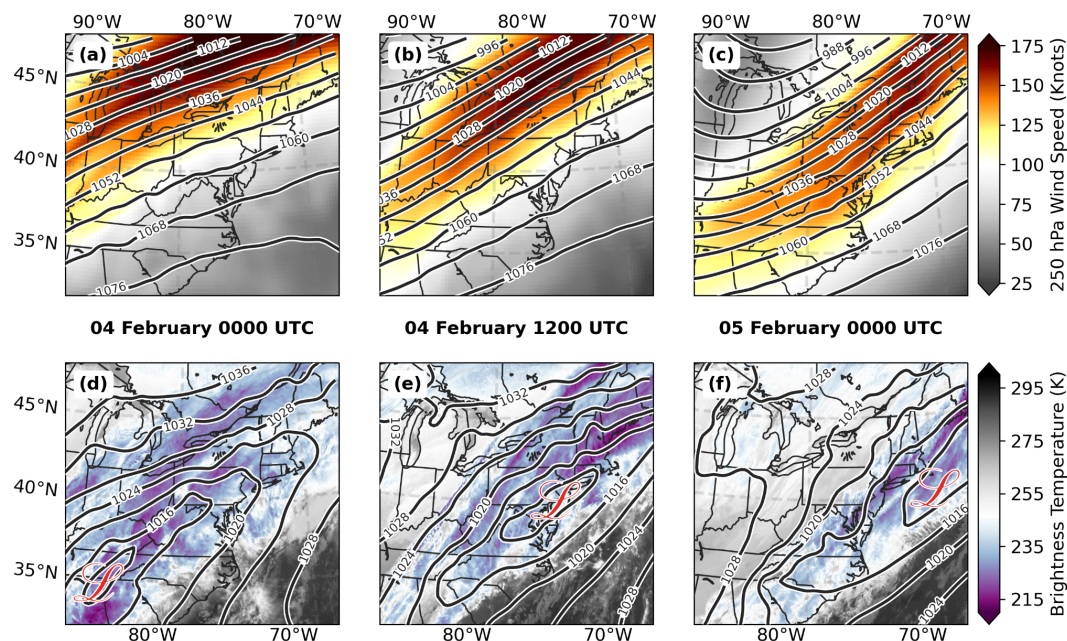
185 For this analysis, we will use IMPACTS observations collected during the 04 February 2022
186 event that delivered wintry-mixed precipitation across a broad region of the northeast US.



187 IMPACTS deployed an in situ (P-3) and remote sensing (ER-2) aircraft. The P-3 aircraft was
188 equipped with instrumentation to measure the in situ cloud microphysical properties and the
189 high-altitude ER-2 aircraft was equipped with nadir-viewing remote sensing instrumentation
190 analogous to those onboard satellite-based platforms (e.g., Skofronick-Jackson et al. 2017). The
191 two aircraft targeted the storm over the coastal New England area where, as an example of the
192 surface precipitation characteristics during this event, the Boston, MA (KBOS) Automated
193 Surface Observing System (ASOS; Brodzik 2022a) reported nearly 32 mm of precipitation in 24
194 hours. Precipitation initially accumulated in the form of light to heavy rain before transitioning to
195 freezing rain at about 1300 UTC, ice pellets by 1600 UTC, and back to freezing rain at about
196 1930 UTC. A transition to snow and continued accumulation occurred on 05 February at KBOS
197 and over most of the New England area.

198 On 04 February, a broad frontal boundary extended from the Gulf of Mexico to Maine. The
199 prolonged period of wintry-mixed precipitation over the northeast US was sustained by
200 isentropic lifting of moisture-rich low-level flow along this front and overrunning a surface layer
201 which, for many areas, remained subfreezing. Over the eastern US, a mean southwesterly flow
202 developed ahead of an initially positively tilted 250-hPa trough at 0000 UTC 04 February that
203 developed to nearly neutral tilt by 0000 UTC 05 February (Fig. 1a-c). An associated jet streak
204 exceeding 150 kts was situated over northern New England such that between about 1200 UTC
205 04 and 0000 UTC 05 February, upper-level divergence in the right entrance region further
206 supported lifting within the atmospheric column (Bjerknes 1951; Uccellini and Kocin 1987;
207 Holton and Hakim 2012). During this time period, a modest elongated southwest-northeast
208 oriented low-pressure minimum of approximately 1010 hPa was maintained over a broad region
209 of coastal New England (Fig. 1d-f).

210



211

212 **Figure 1:** Synoptic evolution of the winter storm that impacted the northeast US: (a-c) 250 hPa
 213 geopotential heights (dam) and wind speeds (knots) and (d-f) mean sea level pressure (MSLP,
 214 hPa) and cloud brightness temperature (K) for the times 0000 UTC 4 February (a, c); 1200 UTC
 215 4 February (b, e) and 0000 UTC 5 February 2022 (c, f). The 250-hPa and MSLP data are from
 216 the European Center for Medium-Range Weather Forecast Reanalysis v5 (ERA5; Hersbach et
 217 al. 2020) and the brightness temperature data are from the Geostationary Operational
 218 Environmental Satellites (GOES) 10.3 μm channel (Brodzik 2022b).

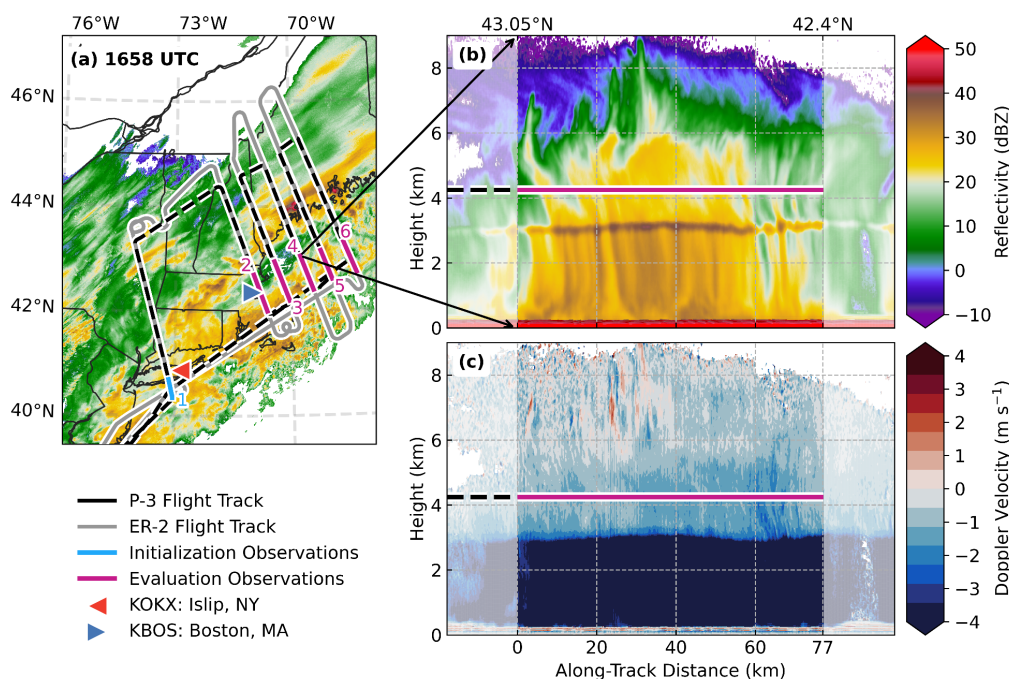
219

220

221 Between about 1300 and 1800 UTC, the P-3 and ER-2 aircrafts flew a “lawnmower-style”
 222 pattern orthogonal to the long axis of an enhanced region of reflectivity while translating
 223 subsequent flight legs to the northeast, such that the storm was sampled in an approximately
 224 Lagrangian manner (Fig. 2a). The P-3 flew its initial flight leg south to north beginning at about
 225 1340 UTC briefly at 6.5 km MSL before descending to a constant altitude of about 6.2 km MSL.
 226 At the southern end, this initial flight leg was near the NWS rawinsonde launch site at Islip, NY
 227 (KOKX). The P-3 descended on each subsequent flight leg to sample different layers of the
 228 cloud reaching an altitude of 3.0 km MSL on the final north-to-south flight leg, which transected
 229 the 0°C melting level. The two enhanced regions of reflectivity, on either side of the surface



230 frontal boundary, exhibited differing cloud and precipitation properties. At the surface, the
 231 northern region of enhanced reflectivity was dominated by snowfall whereas the southern region
 232 was dominated by rain during the period of aircraft sampling then transitioning to wintry-mixed
 233 precipitation. As we describe in Section 2.2, in situ measurements are used to indicate riming,
 234 which was commonly observed over the southern region of enhanced reflectivity but absent over
 235 the northern region. Therefore, to address our science questions, our present analysis is
 236 constrained to measurements of the southern portions of flight legs (Fig. 2a).
 237



238

239 **Figure 2:** IMPACTS operations on 04 February 2022 over the northeast US targeting regions of
 240 enhanced reflectivity that persisted for several hours in the operational National Weather
 241 Service (NWS) Multi-Radar Multi-Sensor (MRMS; Zhang et al. 2011) product. Shown are (a) the
 242 coordinated P-3 and ER-2 flight tracks and MRMS composite reflectivity at approximately mid-
 243 flight (1658 UTC) with subsets for each numbered flight leg at the southern enhanced region of
 244 reflectivity indicating data used for this study. Also indicated in (a) are the NWS rawinsonde
 245 launch site at Islip, NY (KOKX) and ground verification site at Boston, MA (KBOS). Ku-band
 246 reflectivity (b) and Doppler velocity (c) vertical profiles as measured by the ER-2 aircraft from
 247 1628 (north) to 1634 UTC (south) depict the vertical cloud profile across the region of enhanced
 248 reflectivity (between transparent regions) for the fourth flight leg while the P-3 aircraft sampled
 249 in situ at ~4.3 km MSL altitude (magenta line in b, c), ending the flight leg at ~42.4°N.
 250



251

252 **2.2. Observations: Surface Based, Remote Sensing, and In Situ**

253 The initial ER-2 and P-3 flight leg approximately overflew the NWS operational Islip, NY
254 (KOKX) rawinsonde launch site (Fig. 2a). Because of the relatively steady-state nature of the
255 storm during the aircraft sampling period, the KOKX 1200 UTC rawinsonde (Waldstreicher and
256 Brodzik 2022) is used to estimate the atmospheric properties in the southern portion of the flight
257 legs. Because these southern portions of the flight legs were mostly offshore, we use the nearest
258 ASOS measurements at KBOS between 1300 and 1800 UTC to estimate the mean surface
259 precipitation rate for model comparison. The ER-2 aircraft flew well above the storm at
260 approximately 20 km MSL and operated two nadir-viewing radars on 04 February: the dual-band
261 13.9 GHz (Ku-band) and 35.6 GHz (Ka-band) High-Altitude Wind and Rain Airborne Profiler
262 (HIWRAP; Li et al. 2016; McLinden et al. 2022a) and the 94 GHz (W-band) Cloud Radar System
263 (CRS; McLinden et al. 2022b). For radar reflectivity and Doppler velocity measurements of the
264 precipitation, we use HIWRAP measurements, which have a vertical resolution of 150 m and a
265 surface footprint of 1 km. At Ku-band, HIWRAP has a minimum sensitivity of approximately -
266 10 dB at an altitude of 10 km MSL (Li et al. 2016).

267 Of the numerous instruments onboard the P-3 aircraft, those of relevance to this study
268 include cloud Optical Array Probes (OAPs) and those that measure Liquid Water Content
269 (LWC) and vertical air motion. The OAPs provide measurements of the two-dimensional
270 projected sizes, shapes, and concentrations of particles. Data from a Two-Dimensional Stereo
271 (2D-S; Lawson et al. 2006), which is commonly used for measurements of particles smaller than
272 about 1 mm in diameter, are unavailable for the 04 February flight. However, a vertically
273 oriented High-Volume Precipitation Spectrometer (HVPS; Lawson et al. 1993) provided particle
274 measurements at sizes greater than 0.5 mm which were used to construct PSDs. Measurements of
275 LWC were obtained from a Fast Cloud Droplet Probe (FCDP; Lawson et al. 2017) which
276 operated as part of the Hawkeye combination probe. The FCDP uses Mie light scattering
277 principles to size and count liquid water droplets from 2 to 50 μm in diameter, from which
278 number and mass concentrations can be derived. Processing of the OAP and FCDP data was
279 performed by the National Center for Atmospheric Research (NCAR; Bansemer et al. 2022) and
280 is used at a 1 Hz frequency. Vertical air motion measurements were provided by the Turbulent
281 Air Motion Measurement System (TAMMS), which uses several sensors at different locations on



282 the aircraft to estimate the 3D components of the ambient wind (Thornhill et al. 2003). For
283 TAMMS configured to the P-3, the accuracy of vertical winds measurements is estimated to be
284 0.2 m s^{-1} (Thornhill 2022).

285

286 **3. Simulation Design and Validation**

287 **3.1. Model Description**

288 Several bulk microphysics schemes have been developed to more realistically represent the
289 observed continuous evolution of ice-phase particle populations during riming (e.g., Morrison
290 and Milbrandt 2015; Jensen et al. 2017; Cholette et al. 2023). Recently, this modeling approach
291 has been extended to a Lagrangian particle-based scheme in the novel McSnow model (Brdar
292 and Seifert 2018). The particle-based approach affords some advantages over the bulk approach,
293 namely that evolution of a population of particles occurs independent of an Eulerian grid cell
294 structure and is not constrained by assumptions about the PSD. The McSnow model was
295 developed in a 1D columnar configuration and was expressly designed to simulate the evolution
296 of an initial particle population during sedimentation through the column (Brdar and Seifert
297 2018). The notion of a particle in McSnow follows the super-droplet principle (Shima et al.
298 2009) whereby a multiplicity of real particles having commonality among physical properties
299 and location are represented by a single super-particle. These super-particles are continuously
300 introduced in the upper boundary of the model such that initially prescribed PSD characteristics
301 are maintained and then evolve by vapor deposition and aggregation, with an option for riming to
302 occur within a user-defined mixed-phase layer. From 2D simulations using McSnow,
303 DeLaFrance et al. (2024) demonstrated that mixed-phase layer depth significantly modulates
304 surface precipitation rates, varying up to 50% in response to a depth change of 750 m and that in
305 situ measurements of SLW content provide a constraint on the layer's vertical extent. Following
306 riming, melting of the particles occurs as its surface temperature exceeds 0°C , and collision-
307 coalescence processes may then occur, but no additional precipitation mass is generated by
308 warm-rain processes. The thermodynamic profile is prescribed and there are no mechanisms of
309 feedback on the ambient environment based on the microphysical processes.

310 At any point in the column, detailed information about individual particle properties are
311 directly accessible. In general, however, there is greater utility in the description of a population
312 of particles in the form of a binned PSD expressed as the number concentration, N , of particles



313 with diameter, D . We use a construction of 200 bins linearly spaced from 2 μm to 10 cm. From
314 the PSD, radar quantities associated with moments of the PSD are computed by using a forward
315 operator to estimate the radar scattering properties. Several scattering models have previously
316 been adopted to radar scattering from ice crystals, principally differing in the complexity of the
317 scattering particle's geometry. A population of ice crystals may be treated as spheres and
318 scattering computed directly from Mie theory (Bohren and Huffman 1983); however, this
319 approach vastly simplifies the irregular geometry of natural ice crystals. Scattering estimates
320 based on the T-matrix method (Mishchenko et al. 1996) support nonsphericity of particles using
321 a spheroidal shape. Furthermore, the orientation of the spheroids relative to the radar beam may
322 be specified or randomized (Mishchenko and Travis 1998). A more sophisticated approach
323 termed discrete-dipole approximation (DDA) accounts for the complex scattering interactions of
324 irregular crystal geometry (Purcell and Pennypacker 1973) and is therefore a compelling method
325 to estimate scattering of natural crystals. However, for our simulations, crystal habits or detailed
326 properties of particle geometry are not predicted and thus, T-matrix is an apt method of
327 estimating radar scattering. Specifically, we use the PyTMatrix software (Leinonen 2014) to
328 estimate the radar backscattering cross section, σ , and compute Z , defined as:

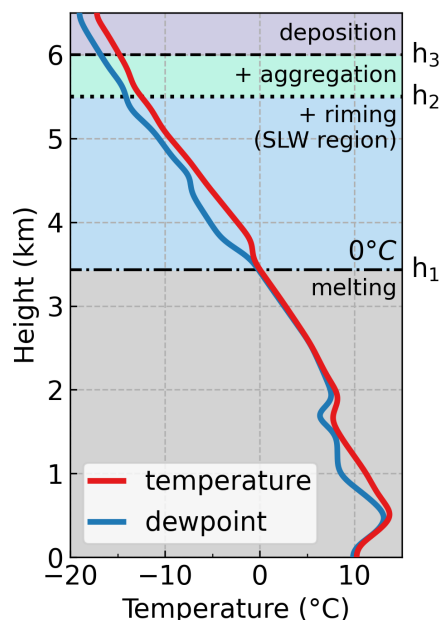
$$329 \quad Z = \frac{\lambda^4}{\pi^5 |K|^2} 10^{18} \int_0^\infty \sigma(D) N(D) dD, \quad (1)$$

330 where λ is the radar wavelength and K is the dielectric factor. From the simulations, we also
331 estimate Doppler velocity, V_D , which is the reflectivity-weighted fall velocity, v , of the particles,
332 defined as:

$$333 \quad V_D = \frac{\int_0^\infty v(D) \sigma(D) N(D) dD}{\int_0^\infty \sigma(D) N(D) dD}. \quad (2)$$

334 For a mixed-phase cloud, Tridon et al. (2019) demonstrated a degradation of skill in T-matrix Z
335 estimates at higher radar frequencies (i.e., Ka- and W-band). To minimize uncertainties
336 associated with non-Rayleigh radar scattering effects (e.g., Matrosov 2007; Liu 2004, 2008), we
337 specify $\lambda = 25$ mm for all calculations, which is comparable to the Ku channel on the HIWRAP
338 radar. Additionally, for consistency with the HIWRAP measurements, a two-way correction for
339 attenuation due to precipitation particles was applied following methodology described in
340 Williams (2022).

341



342

343 **Figure 3:** Schematic of the one-dimensional columnar configuration of the McSnow model with
 344 prescriptive process-based layers for evolution of new particles initiated at the column's upper
 345 boundary. Static temperature and dew point vertical profiles are derived from the 04 February
 346 1200 UTC KOKX rawinsonde.
 347

348

349 3.2. Control Simulation Design

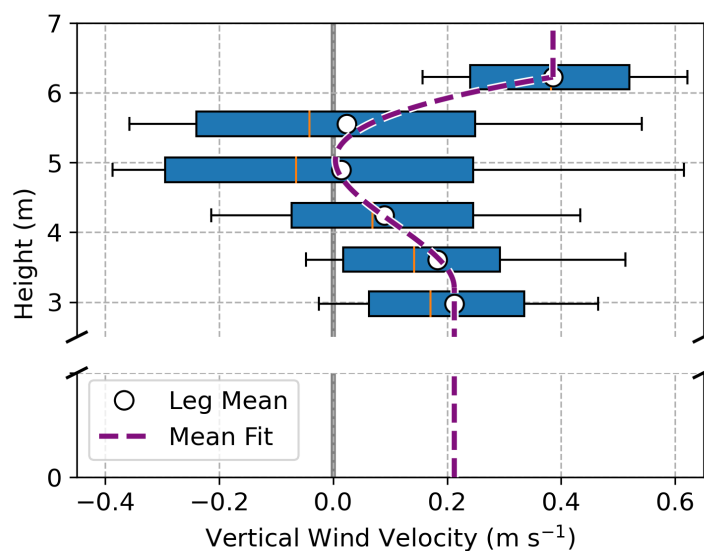
350 We use the in situ measurements combined with rawinsonde data to construct a quasi-
 351 idealized cloud profile that is representative of the mean state of the 04 February storm which we
 352 apply prescriptively in the 1D columnar McSnow model. The process-based model design is
 353 illustrated by the schematic in Fig. 3. Introduction of new particles from a prescribed PSD occurs
 354 at 6.5 km MSL, which approximately corresponds to the uppermost height of in situ
 355 observations. Dominant particle types observed at this height were side planes and bullet
 356 rosettes. As newly introduced particles undergo sedimentation, growth occurs initially by vapor
 357 deposition only. Aggregation is introduced at 6 km MSL (-15°C) since aggregate particles,
 358 mostly side planes and other planar crystals, were present in observations below 6 km MSL.
 359 Riming is introduced at 5.5 km MSL, which we approximate as an upper extent of the mixed-
 360 phase layer based on the presence of SLW droplets and rimed particles beginning at flight leg 3



361 (4.9 km MSL) and, subsequently, on legs 4 and 5 (4.3 and 3.6 km MSL). The onset of melting is
362 determined by the thermodynamic profile which is obtained from the 1200 UTC KOKX
363 rawinsonde. Although model processes are largely independent of an Eulerian grid (see
364 discussion in Brdar and Seifert 2018, Section 2), model output and analysis occurs on a gridded
365 column with 500 vertical levels, which yields a vertical resolution of 13 m. Additionally, we
366 specify a time step of 5 s and total run duration of ten hours; results are analyzed as averages
367 over the final five hours, after the system has reached a steady state.

368 As a constraint on the observational data used for simulation construction, we approximate
369 the horizontal extent of the southern region of enhanced reflectivity by visually assessing its
370 lateral edges during each flight leg using the Ku-band radar vertical profiles. An example of this
371 approach is provided in Fig. 2b, c for the fourth flight leg in which data used is from the center
372 portion of the figure. The boundaries (opaque regions) varied for each flight leg, adapting to the
373 northeastward progression of the storm and translation of each flight leg. The initial PSD
374 characteristics are derived from an average of the measurements on the uppermost height flight
375 leg at ~6.5 km MSL between the southern end point of the leg and 40.7°N latitude (see Fig. 2a).
376 Because measurements are unavailable for particles smaller than 0.5 mm, we fit a Gamma
377 distribution to the mean PSD from HVPS measurements and then extend the fitted distribution to
378 a lower size limit of 112.5 μm to estimate an IWC of 0.14 g m^{-3} and total number concentration,
379 N , of $23 \times 10^3 \text{ m}^{-3}$. For all simulations, an initial super-particle multiplicity of 10^5 in the upper
380 boundary is specified. We assume that newly initialized particles at 6.5 km MSL have a mass-
381 dimension relationship of $m = 0.00294D^{1.94}$ (cgs units) following Brown and Francis (1995), for
382 unrimed aggregate ice crystals in a stratiform cloud. From analysis of four IMPACTS events
383 during the preceding 2020 deployment, Heymsfield et al. (2023) showed that Z calculated from a
384 PSD using the Brown and Francis (1995) mass-dimension relationship and a T-matrix approach
385 yielded an agreement with observations at Ku band within 1.15 dB.

386



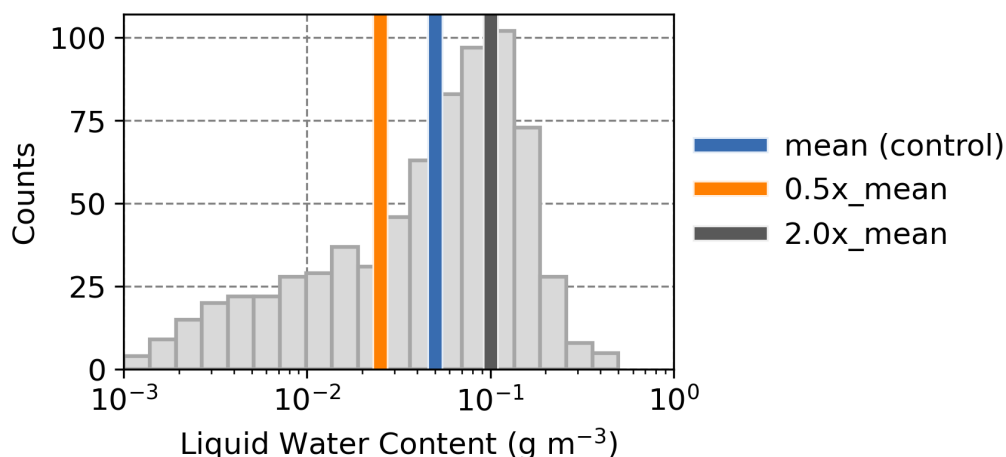
387

388 **Figure 4:** Vertical wind velocity measurements from the Turbulent Air Motion Measurement
 389 System (TAMMS) during P-3 flight legs indicating lower to upper quartiles in the boxed regions,
 390 10th and 90th percentiles at the whiskers, and medians at the vertical lines. A mean profile is
 391 fitted to the flight-level mean values (white markers).
 392

393

394 Falling particles are subject to an updraft. We estimate a mean-state vertical wind profile by
 395 fitting a third-degree polynomial curve to the mean measurements from each flight leg and
 396 extending the upper- and lower-most measurements as a constant value to heights beyond the
 397 observation altitudes (violet curve in Fig. 4). Within the mixed-phase layer (h_2 to h_1 in Fig. 3),
 398 SLW properties are derived collectively using FCDP measurements on flight legs 3, 4, and 5. We
 399 uniformly prescribe the mean values for SLW concentration of 0.05 g m^{-3} (Fig. 5) and a
 400 characteristic droplet diameter of $22 \text{ }\mu\text{m}$ within the mixed-phase layer.
 401

401



402

403 **Figure 5:** Histogram of liquid water content (LWC) measurements from the Fast Cloud Droplet
 404 Probe (FCDP) during P-3 flight legs through mixed phase cloud (4.9 to 3.6 km MSL). Vertical
 405 bars indicate mean (0.05 g m⁻³) and perturbed-state values used for sensitivity simulations scaled
 406 from the mean by factors of 0.5 and 2.0.
 407

408

409 Although we prioritize the use of observations for model constraint, several decisions are
 410 necessary regarding the parameterizations of modeled processes. With two exceptions, these
 411 parameterization decisions follow those discussed in DeLaFrance et al. (2024, see Section 2.3
 412 and Appendix A). The first difference regards the aggregation process. Upon collision of two or
 413 more particles, a sticking efficiency parameter which scales from 0 to 1 is used to describe the
 414 probability of the particles merging, where an efficiency of 1 will always yield a union. The
 415 sticking efficiency parameterization follows Connolly et al. (2012), which is dependent on
 416 temperature and maximizes at -15°C. In testing, however, we found that the maximum likelihood
 417 estimate (MLE) values of Connolly et al. (2012; see Fig. 14b) yielded lower concentrations of
 418 large particles than were observed. Alternatively, use of a higher efficiency value inspired by the
 419 upper extent of their confidence interval yielded a more observationally-consistent PSD
 420 evolution and maximum particle sizes. Therefore, aggregation is introduced at 6 km MSL (Fig.
 421 3) with a sticking efficiency of 0.9 at -15°C and linearly decreases to 0.5 at -10°C, remaining
 422 constant at 0.5 between -10° and 0°C. The second parameterization decision which differs from
 423 DeLaFrance et al. (2024) regards riming where a continuous approach was used in favor of a



424 stochastic approach, although they describe only minor differences between the two approaches.
425 In the present analysis, we find a slightly reduced collection of rime mass using the continuous
426 parameterization when compared to the stochastic parameterization. Applying the continuous
427 parameterization approach, particles accumulate a mean rime fractional mass of 0.49 by the time
428 they reach 3.6 km MSL (flight leg 5, immediately above the melting level), whereas applying the
429 stochastic parameterization, a rime fractional mass of 0.55 is accumulated. Visual assessment of
430 the in situ particle imagery indicated that the stochastic method produces a more observationally
431 consistent riming evolution. Therefore, the stochastic riming parameterization is used in all
432 simulations.

433

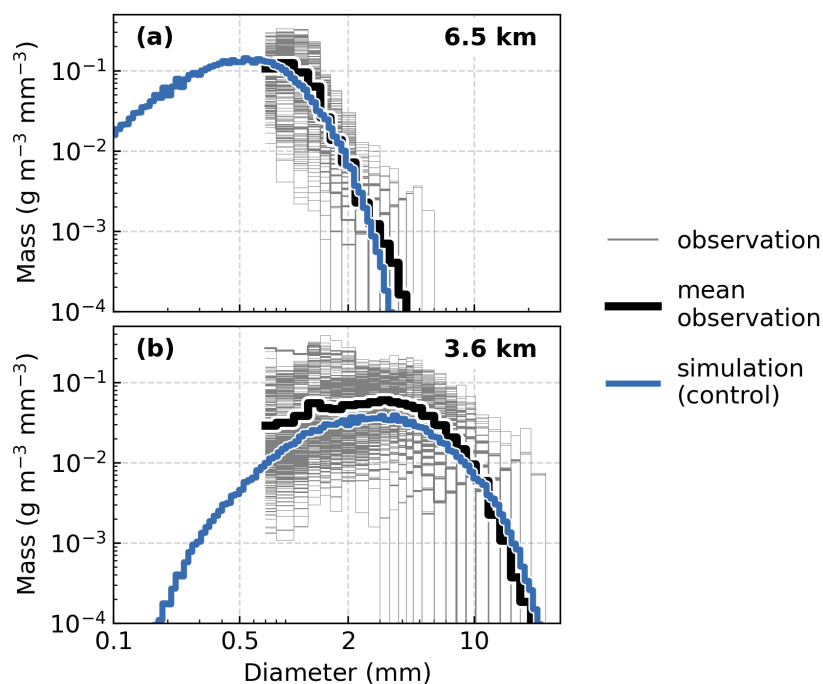
434 **3.3. Control Simulation Assessment**

435 The objective for a control simulation is to produce an evolution of a population of particles
436 within a vertical column that is physically consistent with the observed cloud profile. In Fig. 6,
437 we compare the control simulation PSD to the mean observed PSD ($D \geq 0.7$ mm). Although PSD
438 measurements at smaller particle sizes are unavailable for this flight, the approximately
439 Lagrangian aircraft sampling yielded a temporally consistent evolution of the PSD at larger sizes.
440 Measurements from flight leg 1 are used to assess the simulation during the particle initialization
441 stages within the uppermost region of the model, whereas measurements collected downstream
442 on flight legs 2 through 6 are used to assess simulation performance during the later stages of
443 particle evolution. The model produces an initial particle population at 6.5 km MSL (Fig. 6a) that
444 is consistent with the mean observations at large particle sizes and follows the assumed Gamma
445 distribution form at small sizes. Flight leg 5 (Fig. 2a), at approximately 3.6 km MSL, was the
446 lowest altitude flown before reaching the melting level. At this altitude, evaluation of the
447 simulation shows skill in evolving this initial particle population by deposition, aggregation, and
448 riming processes throughout a nearly 3 km-deep cloud layer.

449 Particle growth between 6.5 km (Fig. 6a) and 3.6 km MSL (Fig. 6b) through aggregation and
450 to a lesser extent, depositional growth, is expressed in the shift of the observed PSD to larger
451 particle sizes. This evolutionary characteristic is reproduced by the control simulation although
452 slightly larger maximum particle sizes are generated, and the ice mass may be underrepresented
453 among particles smaller than about 2 mm in diameter. We note, however, that sizing uncertainty
454 in the observed measurements is greater at these small sizes owing to the relatively coarse pixel



455 resolution of 150 μm for the HVPS probe (Bansemer et al. 2022). To further validate the control
 456 simulation and to assess the continuous particle evolution throughout the vertical profile, Z is
 457 estimated from the simulated PSD and compared to the HIWRAP Ku-band measurements.
 458



459

460 **Figure 6:** Particle size distributions (PSDs) of ice mass for observed 1 Hz and mean values
 461 derived from (a) P-3 flight leg 1 at 6.5 km MSL and (b) flight leg 5 at 3.6 km MSL (see Fig. 2)
 462 and for the control simulation at equivalent altitudes.

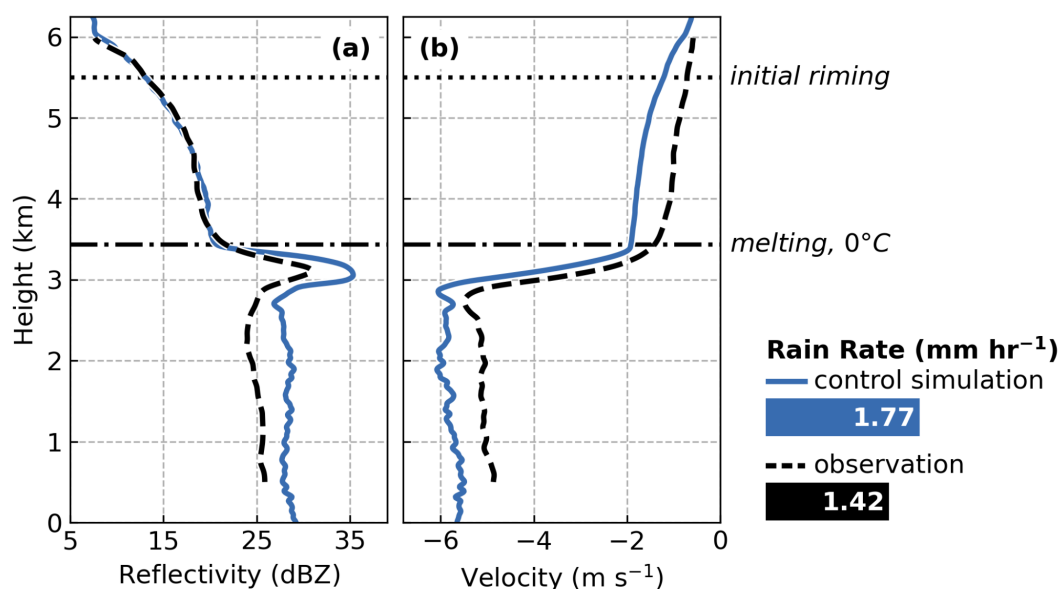
463

464

465 Figure 7 shows the median observed vertical profile of Z and V_D computed from the
 466 downstream flight legs 2 through 6, as indicated in Fig. 2a. Data from the lowest 500 m were
 467 removed due to noise from ground clutter. From the observed vertical profiles, several inferences
 468 are made about the microphysical processes. Beginning at 6 km MSL, Z rapidly increases with
 469 descent, which is expected with an onset of aggregation. The rate of increase in Z with
 470 descending height reaches a relative maximum near 5.5 km MSL (Fig. 7a), coincident with an
 471 apparent acceleration of V_D . Within the subsequent 1 km (5.5 km to 4.5 km MSL), V_D increases



472 from -0.72 m s^{-1} to -1.00 m s^{-1} (Fig. 7b). This effect is assumed to be associated with the onset of
 473 riming, and subsequently, changes in particle densities. Particle melting begins near 3.4 km
 474 MSL, at which point a bright band signature is apparent and V_D rapidly increases. Below the
 475 bright band, Z remains nearly constant at about 25 dBZ and V_D is about -5 m s^{-1} .
 476



477

478 **Figure 7:** Vertical profiles of (a) radar reflectivity and (b) Doppler velocity at Ku band for the
 479 control simulation (blue lines) and observed (dashed black lines) median from ER-2 HIWRAP
 480 radar during flight legs 2-6 (see Fig. 2a, magenta segments). Data for the observed profile below
 481 500 m MSL are omitted due to ground clutter. A dotted line at 5.5 km MSL indicates the onset of
 482 riming and a dash-dotted line indicates the 0°C height. Also shown at the right are the surface
 483 rain rate values from the control simulation (blue) and observed at KBOS (black) between 1300
 484 and 1800 UTC on 04 February 2022; horizontal bar lengths illustrate magnitude differences.
 485

486

487 The vertical profile of Z is well reproduced by the control simulation, particularly above the
 488 melting level (Fig. 7a), which suggests confidence in its prescriptive configuration. Upon
 489 melting, Z is overestimated by the control simulation and maintains a bias of about 2 to 5 dB
 490 throughout the warm layer. While an evaluation of warm-rain processes is beyond the scope of
 491 the present study, it is possible that this overestimate in Z results from an incomplete
 492 representation of warm-rain processes by the model, such as droplet breakup and shedding, or



493 from uncertainties in the scattering estimates. Confirmation of an attributable mechanism would
494 be challenging without in situ observations below the melting level. Rain rates at the surface are
495 one common model validation metric. Because the aircraft sampling occurred primarily offshore
496 (see Fig. 2a), an ideally situated ground site is unavailable. However, we find comparison with a
497 nearby ground site useful towards determining whether the control simulation produces
498 physically realistic estimates that are representative of the rainfall across the broader region. At
499 the surface, during aircraft sampling (1300 to 1800 UTC), the nearest ground site, KBOS,
500 reported a rain rate of 1.42 mm hr⁻¹. The control simulation produces about 25% more surface
501 rain with an average rain rate of 1.77 mm hr⁻¹.

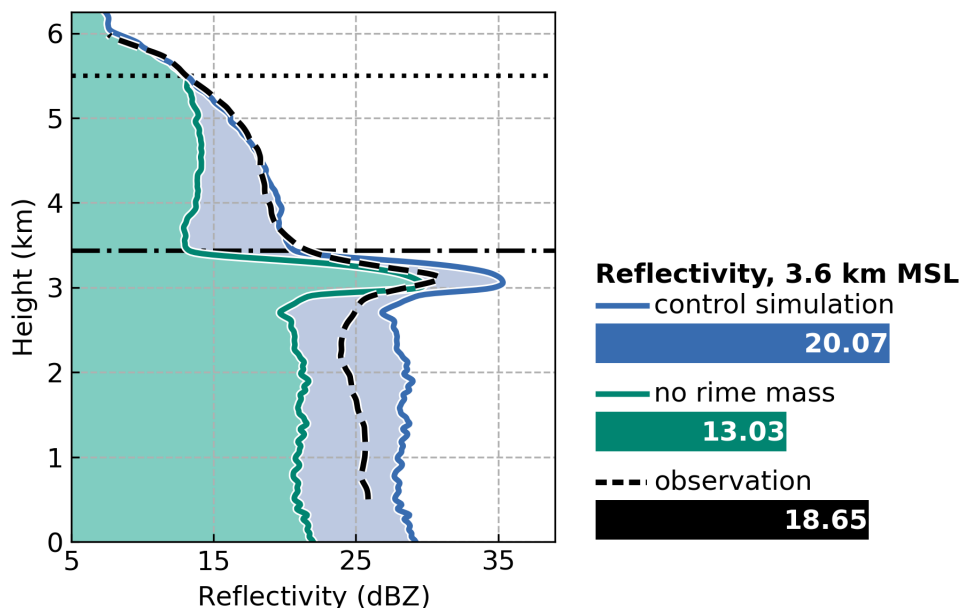
502 Despite the confidence in Z aloft, we find that V_D is underestimated by about 0.5 to 1 m s⁻¹ in
503 the control simulation but are within an uncertainty range of ± 1 m s⁻¹ (Matthew McLinden,
504 personal communication, 25 April 2024) for the HIWRAP Ku-band V_D measurements. This bias
505 between the observed and simulated V_D is consistent throughout the column, suggesting that this
506 consistent bias may be explained, to a large extent, by uncertainty in the observations. More
507 importantly for this analysis, the relative changes in V_D with height, which have process-based
508 implications, are similar between the observed and simulated profiles.

509

510 **4. Process-Based Contributions and Sensitivities on Doppler Radar Vertical Profiles**

511 A principal advantage of the particle-based design of the McSnow model is that information
512 about microphysical properties is retained by the model at the scale of the individual particles.
513 For particles in the control simulation, the onset of riming at 5.5 km MSL (h_2 in Fig. 3) initiates a
514 change in the physical evolution of the particle with subsequent sedimentation. At 3.6 km MSL,
515 the particles have accumulated a mean rime fractional mass of 0.55, increasing the total
516 precipitation mass and accelerating its fallout rate. Radar scattering by the particle, expressed
517 through Z , is also modified by rime accumulation, yet these effects are difficult to distinguish
518 from concurrent processes, including deposition and aggregation. To investigate these scattering
519 implications, we estimate the vertical profile of Z with and without contributions of rime mass.

520



521

522 **Figure 8:** As in Fig. 7a but with an added vertical profile (in green) for estimated reflectivity (Z)
 523 with particle rime mass removed. Shown at the right are simulated and observed Z values
 524 computed at 3.6 km MSL; horizontal bar lengths illustrate magnitude differences.
 525

526

527 Figure 8 compares Z from the control simulation (as in Fig. 7a) to an unrimed estimate of Z
 528 obtained by subtracting the rime mass from the particles and recomputing their scattering
 529 properties. Removal of rime mass appears to significantly impede further increases in Z with
 530 descending height below 5.5 km MSL. Near the melting level, Z is reduced from 20.07 to 13.03
 531 dBZ between the control and simulation and the unrimed estimate, suggesting that the
 532 accumulated rime mass contributes to about 35% of the total Z (in dB units). This calculation,
 533 however, only considers the implications of riming on radar scattering; the complex interactions
 534 of concurrent processes are neglected by solely removing the rime mass from evolved particles
 535 in the control simulation. Additionally, the effects on V_D , which manifest cumulatively during
 536 riming, cannot be investigated in the same manner. To explicitly investigate the effects of riming
 537 on the radar profiles, and to distinguish these effects from concurrent processes, we introduce
 538 several sensitivity simulations which independently perturb the riming or aggregation processes.
 539

539



Simulation	Description	Perturbation Assignment
control	Observation-based mean-state simulation	none
high_SLW	Increase SLW by 2.0 from control	0.100 g m ⁻³ LWC
low_SLW	Reduce SLW by 0.5 from control	0.025 g m ⁻³ LWC
no_riming	Remove riming to distinguish effects from aggregation	Riming process turned off
MLE_C12_agg	Reduce aggregation from control to moderate efficiency	MLE sticking efficiency; see Fig. 14, Connolly et al. (2012)
low_C12_agg	Reduce aggregation from control to low efficiency	0.5 x MLE sticking efficiency; see Fig. 14, Connolly et al. (2012)

540

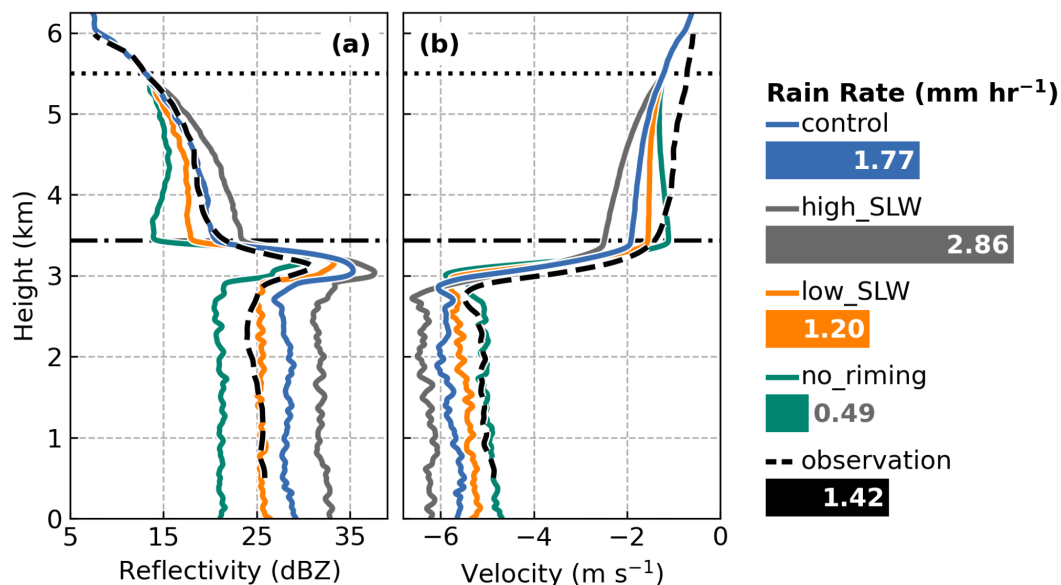
541 **Table 1:** Descriptions and perturbations relative to the control simulation applied for each
 542 simulation.

543

544

545 Although the southern regions of the 04 February 2024 event were predominantly stratiform,
 546 variations in the mixed-phase layer LWC were observed (Fig. 5). Within sufficiently deep
 547 mixed-phase layers, prior model simulations have demonstrated that small (e.g., < 0.05 g m⁻³)
 548 perturbations in LWC alter particle fallout characteristics which can yield substantial increases or
 549 decreases in the surface precipitation rate (DeLaFrance et al. 2024). Here, we similarly introduce
 550 two sensitivity simulations perturbing LWC within the mixed-phase layer (h_1 to h_2 in Fig. 3),
 551 within the range of observed LWC (Fig. 5). In the control simulation, we prescribed the mean
 552 observed LWC value of 0.05 g m⁻³. A scaling factor of two relative to the control is used to
 553 prescribe a high concentration (0.1 g m⁻³) for the “high_SLW” simulation and low concentration
 554 (0.025 g m⁻³) for “low_SLW” concentration. As a limiting case which is analogous to the
 555 removal of rime mass (Fig. 8), we construct a “no_riming” simulation with the riming process
 556 inactive. A brief summary of these riming sensitivity simulations is provided in Table 1.

557



558

559 **Figure 9:** As in Fig. 7 but for the control and riming-based sensitivity simulations: *high_SLW*,
 560 *low_SLW*, and *no_riming*. At the right are surface simulated and observed surface rain rate
 561 values; horizontal bar lengths illustrate magnitude differences.

562

563

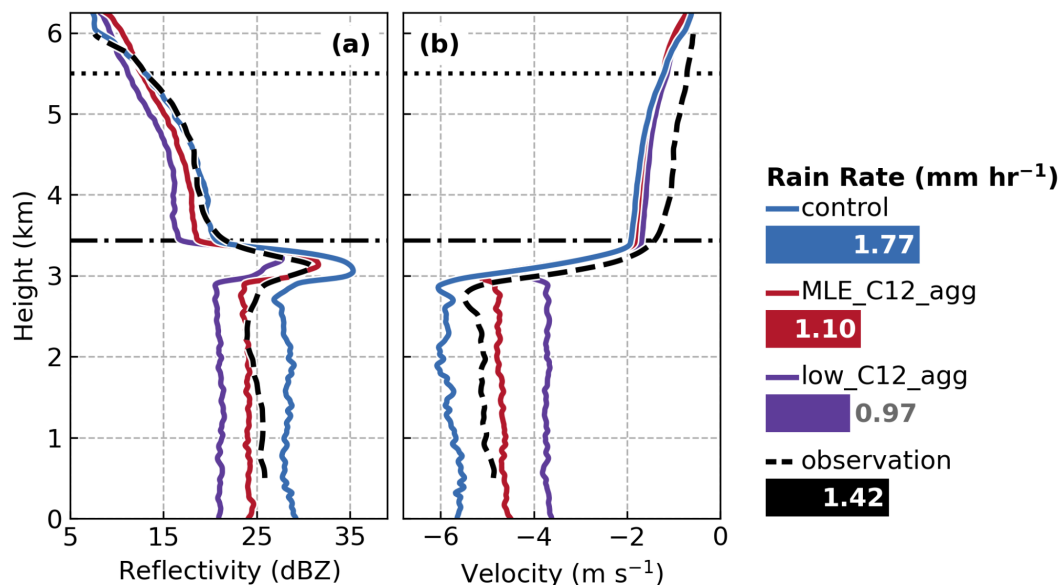
564 Vertical profiles of Z and V_D for the *high_SLW*, *low_SLW*, and *no_riming* sensitivity
 565 simulations relative to the control are shown in Fig. 9. Complete removal of the riming process
 566 in the no riming simulation (Fig. 9a) produces a similar Z profile as found by computing Z for
 567 equivalent unrimed particles from the control simulation (Fig. 8). This result underscores the
 568 significant sensitivity of Z to changes in particle mass during riming, despite concurrent
 569 microphysical processes. Perturbing LWC by a factor of 2 in the *high_SLW* or 0.5 in the
 570 *low_SLW* simulations relative to the control produces opposing, but similar in magnitude,
 571 changes in Z (Fig. 9a), indicating a regularity in the response of Z to SLW variability. Similarly,
 572 the effects of SLW variability on V_D demonstrate a regular response (Fig. 9b). We note that these
 573 simulation responses in Z and V_D to SLW variability assume that the particles are well mixed
 574 such that probabilistic collision of ice crystals and SLW droplets is the same throughout the
 575 layer.

576 In the *high_SLW* simulation, the rate of further V_D acceleration with descent below 5.5 km
 577 MSL is nearly doubled relative to the control. Conversely, below about 5 km MSL, further



578 increases in V_D cease in the low_SLW simulation and decrease in V_D occurs in the no_riming
579 simulation. The competing effects of riming and aggregation processes on V_D manifest in the
580 low_SLW and no_riming simulations; riming accelerates the V_D with mass accumulation
581 whereas in the absence of riming, further aggregation yields larger, lower density particles with
582 reduced fall speeds. Consequently, vertical profiles of V_D may provide an insight into dominant
583 microphysical processes, which is consistent with the notion that rimed particles occupy a
584 distinct region of the Doppler spectra (Kalesse et al. 2016). To advance the differentiation of
585 particles evolved by riming, it is necessary to first consider relative effects of variability in the
586 aggregation process.

587 In our development of the control simulation for the 04 February 2022 event, the aggregation
588 process was initially assumed to follow a temperature dependent sticking efficiency identified as
589 the MLE by Connolly et al. (2012; see Fig. 14b). Comparison with in situ PSDs indicated that
590 the MLE sticking efficiency parameter was insufficient to generate observed concentrations of
591 large particles, motivating the use of an increased sticking efficiency in the control simulation.
592 However, to elucidate the effects of aggregation efficiency on radar profiles, we now consider a
593 sensitivity simulation, “MLE_C12_agg”, which follows the MLE sticking efficiency of Connolly
594 et al (2012). Additionally, analogous to the design of the riming sensitivity simulations, we
595 introduce a “low_C12_agg” simulation for which the sticking efficiency is further reduced from
596 the MLE estimate by a factor of 0.5. Relative to the control simulation, the reduction in sticking
597 efficiency in the MLE_C12_agg and low_C12_agg sensitivity simulations lack observational
598 consistency with the presently analyzed 04 February 2022 event. However, it is useful to
599 consider the implications of a realistic range of variability in the aggregation process efficiency
600 to inform general distinctions from the effects of riming within vertical profiles of Z and V_D .
601



602

603

604

605

606

607

608

609

610

611

612

613

614

615

616

617

618

619

620

Figure 10: As in Fig. 7 but for the control and aggregation-based sensitivity simulations: *MLE_C12_agg*, and *low_C12_agg*. At the right are surface simulated and observed surface rain rate values; horizontal bar lengths illustrate magnitude differences.

Figure 10 shows the vertical profiles of Z and V_D for the aggregation efficiency sensitivity simulations, *MLE_C12_agg* and *low_C12_agg*. Reducing aggregation efficiency suppresses the generation of large particles and because of the strong dependency of radar backscatter on particle size, Z decreases relative to the control (Fig. 10a). Additionally, smaller aggregate particles become smaller targets for collision with SLW droplets to accumulate rime mass, which also reduces Z . The latter effect manifests in the reduced surface rain rates, decreasing by 38% in the *MLE_C12_agg* (1.10 mm hr^{-1}) and 45% in the *low_C12_agg* (0.97 mm hr^{-1}) simulations relative to the control (1.77 mm hr^{-1}). Conversely, a reduction in aggregation efficiency has a minimal effect on V_D for ice-phase particles (Fig. 10b). Above the melting level, at 3.6 km MSL, V_D in the *MLE_C12_agg* simulation is reduced from the control simulation by 0.08 m s^{-1} and in the *low_C12_agg*, reduced by 0.24 m s^{-1} . This relative insensitivity of V_D to aggregation arises despite these sensitivity simulations assessing a broad range of possible sticking efficiencies. For example, at -15°C , the sticking efficiency is reduced from 0.9 in the control to 0.32 in the



621 low_C12_agg simulation and at -10°C , from 0.5 in the control to 0.12 in the low_C12_agg
622 simulation.

623 Below the melting layer, however, the effects of aggregation on V_D become significant,
624 decreasing by approximately 2 m s^{-1} between the control and low_C12_agg simulations.
625 Similarly, the surface rain rate decreases by about 45% between the control and low_C12_agg
626 simulations. Thus, despite the significant implications of the aggregation process on precipitation
627 production and its fallout, its variations are not readily perceived in vertical profiles of V_D . This
628 finding significantly differs from the robust sensitivity of V_D to variations in the riming process.
629 While variations in the aggregation and riming processes may manifest similarly in vertical
630 profiles of Z , we find that V_D is uniquely sensitive to riming. Thus, vertical profiles of V_D show
631 promise in identification of riming as a dominant ice-phase microphysical process, which is
632 ambiguous in profiles of Z , only.

633

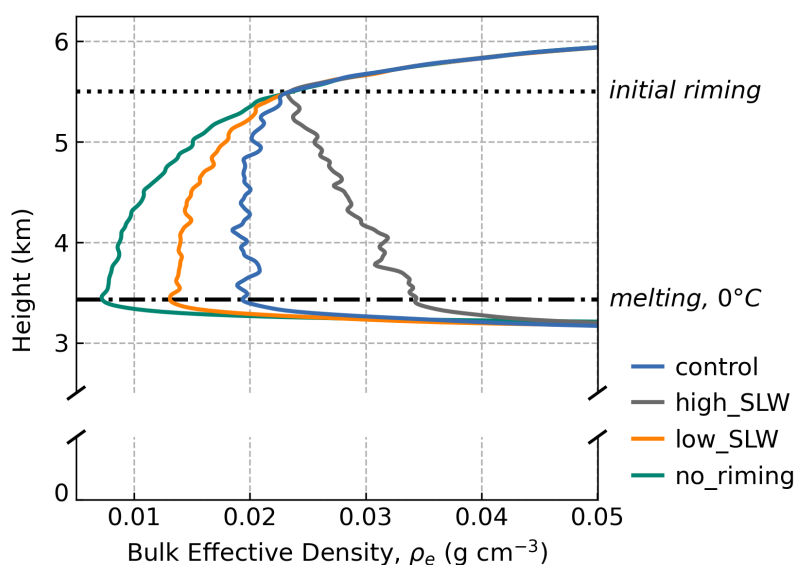
634 5. Discussion

635 Sensitivity in vertical profiles of both Z and V_D owing to rime accumulation rates were
636 previously shown by Kalesse et al. (2016) from bin model simulations by prescribing a fixed
637 vertical profile of LWC then testing two different riming efficiency parameterizations. Their two
638 simulations yielded similar vertical gradients in Z and V_D profiles but with differences in
639 magnitude. They attributed these differences to assumptions about the physical morphology of
640 the ice crystals with accretion of rime mass that had implications for their scattering properties.
641 In our study, we uniquely provided an observational constraint to establish a control state
642 simulation and modeling framework for assessing impacts of riming and aggregation
643 independently. By selecting a fixed riming parameterization for all simulations using this
644 framework, we were able to assess Z and V_D sensitivities attributable to LWC perturbations
645 within the range of observed variability. We found that a small ($\leq 0.05\text{ g m}^{-3}$) range of
646 perturbations in the LWC produced substantial changes in the surface precipitation rate and a
647 corresponding sensitivity in vertical profiles of Z and V_D .

648 The sensitivities expressed in Doppler radar profiles to LWC perturbations is tied to the
649 impact on bulk microphysical properties, especially particle density, ρ_e . In the deposition- and
650 aggregation-prescribed region above 5.5 km MSL (Fig. 11), ρ_e rapidly decreases with
651 descending height due to the efficient aggregation of increasingly open particle geometry. At 5.5



652 km MSL, riming is introduced and ρ_e approaches 0.02 g cm^{-3} , remaining nearly constant until the
 653 melting level as a result of the competing effects of aggregation and riming. In the high_SLW
 654 simulation, the effects of riming dominate whereby the gradient in ρ_e abruptly increases with
 655 descending height. Conversely, in the low_SLW and no_riming simulations, the effects of
 656 aggregation continue to dominate and ρ_e further decreases.
 657



658

659 **Figure 11:** Vertical profiles of bulk effective density, ρ_e , for the evolved particle population for
 660 the control simulation and three riming-based sensitivity simulations described in Section 4:
 661 high_SLW, low_SLW, and no_riming. Calculations of ρ_e assume equivalent spherical volumes of
 662 the particles following Heymsfield et al. (2004).
 663

664

665 Despite the opposing process-based effects on the evolution of ρ_e with height, our
 666 simulations suggest that the effects of aggregation and riming are not readily distinguished by Z
 667 from a Ku-band radar band alone. Riming may be detectable, however, from three-wavelength
 668 (Ku-, Ka-, and W-band) radar by leveraging differential attenuation effects. In prior idealized
 669 modeling simulations for rimed particle growth scenarios, Leinonen and Szyrmer (2015)
 670 identified unique signatures of riming by comparing dual-wavelength ratios (DWR) between Ka
 671 and W bands with DWR at Ku and Ka bands. However, they found the magnitude of this
 672 signature to be modest and proposed that it would likely be difficult to accurately distinguish in



673 observational data. Mason et al. (2019) later investigated the use of triple-frequency Doppler
674 radar measurements from mixed-phase clouds during wintertime snow events to constrain the
675 retrievals of bulk microphysical properties, including the PSD shape factor and ρ_e . They found
676 that triple-wavelength Z measurements effectively constrained the PSD shape parameter, but did
677 not constrain ρ_e . Rather, V_D measurements were necessary to identify transitions to rimed growth
678 cloud regions and provide constraint on ρ_e . Our findings demonstrate that this constraint on ρ_e is
679 attributable to the unique density-dependent response in V_D expressly owing to variations in the
680 riming process within mixed-phase cloud layers with concurrent riming and aggregational
681 growth. Further, our findings suggest that, when combined with Z , coincident vertical profiling
682 measurements of V_D have utility towards diagnosing riming as a dominant process within
683 stratiform clouds from a single-wavelength radar.

684

685 **6. Conclusions**

686 The evolution of ice-phase precipitating particles within a mixed-phase stratiform cloud was
687 simulated to evaluate the effects of riming on the PSD moments and assess the process-based
688 implications on Doppler radar vertical profiles. In situ and remote sensing airborne observations
689 collected during the IMPACTS field campaign for a prolonged wintry-mixed precipitation event
690 over the northeast US on 04 February 2022 were used to design and constrain a quasi-idealized
691 1D mean-state control simulation. Using the Lagrangian particle-based McSnow model, we
692 defined an initial population of ice particles based on in situ measurements in the upper portion
693 of the cloud. As those particles fell, initial evolution occurred by vapor deposition followed by
694 subsequent additions of aggregation and then riming within prescriptive observation-based
695 layered regions. Radar scattering properties were estimated using a T-matrix forward operator
696 and vertical profiles of Z and V_D were computed from the evolved PSD, then evaluated through
697 comparisons with the airborne radar data. The effects of riming on PSD moments expressed
698 through Z and V_D were assessed from simulations which introduce small perturbations in cloud
699 LWC within a range of observed variability. To distinguish effects of riming and aggregation,
700 two additional sensitivity simulations were introduced to determine the unique implications of
701 aggregational growth efficiency on Z and V_D . Through these approaches, we found:

702



- 703 • Ice-phase precipitation particle evolution in a mixed-phase wintertime storm cloud is well
704 constrained by the 1D quasi-idealized McSnow model.
- 705 • Despite modest supercooled liquid water concentrations, rime accumulation is estimated
706 to account for 55% of particle mass generated above the melting level, dominating ice-
707 phase contribution to precipitation rates.
- 708 • Riming cumulatively increased radar reflectivity above the melting level by an estimated
709 6.1 dB and Doppler velocity by 0.9 m s^{-1} and demonstrated significant sensitivity to small
710 perturbations in supercooled liquid water concentrations.
- 711 • Vertical profiles of radar reflectivity demonstrate similar sensitivities to riming and
712 aggregation, but Doppler velocity is uniquely sensitive to riming-based perturbations
713 through changes in particle density.

714

715 Constraining parameterized treatments of rimed particle evolution in numerical models is a
716 known source of uncertainty in simulations of precipitation from bulk-, bin- and Lagrangian
717 particle-based models (e.g., Lin and Colle 2011; Jensen and Harrington 2015; Jensen et al. 2017;
718 Brdar and Seifert 2018). One objective of our analysis was to address this constraining need
719 through quantifying precipitation sensitivities to riming in model simulations based on an
720 observed range of variability in LWC. We found a difference of about 6% in rime fractional
721 mass accumulation in our control simulation whether using a continuous or a stochastic
722 representation of riming with the McSnow model. This effect was expressed within a modeling
723 framework using a quasi-idealized and steady-state 1D column with a homogeneous mixed-
724 phase layer. This approach was appropriate for our intentionally selected region of the observed
725 storm because of its idealistic layered vertical structure apparent in radar observations (Fig. 2b,
726 c), along with its known presence of SLW based on in situ observations. However, in reality,
727 processes are not neatly initiated at distinct levels (e.g., in convective areas). It is expected that
728 increasing ambiguity exists in distinguishing concurrent microphysical processes in these
729 scenarios and, thus, our analysis did not assess the full natural range of complexity in mixed-
730 phase precipitation processes.

731 While model schemes have become increasingly sophisticated, it is not clear that uncertainty
732 in ice-based precipitation estimates have necessarily reduced, highlighting the need for judicious
733 use of observations to advance constraints on modeled processes (e.g., Morrison et al. 2020).



734 Because of the capacity for explicit process representation at the scale of individual particles,
735 Lagrangian models (e.g., McSnow) may be ideally suited to addressing these challenges,
736 especially when combined with datasets which prioritize observations that are consistent with the
737 evolution of particles. This observational consideration was favored during the 04 February 2022
738 event, which was sampled by IMPACTS in an approximately Lagrangian manner. In this study,
739 we focused on riming as a primary ice-phase process, but the northern region of the sampled
740 storm observed significantly less SLW and rime accumulation, presenting a unique natural
741 laboratory for evaluation of modeled aggregation. Sticking efficiencies during aggregation are
742 highly uncertain and difficult to constrain from laboratory experiments (e.g., Connolly et al.
743 2012) yet, as we demonstrated in our study, have significant implications for the accuracy of
744 simulated Z and rain rates. Ongoing work involves curating the in situ measurements of particle
745 evolution within this northern storm region to constrain Lagrangian particle-based simulations
746 and assess the ambient environmental dependencies (i.e., temperature, water supersaturation) and
747 ranges of sensitivities associated with modeled aggregation.

748

749

750 **7. Data Availability Statement**

751 All field observation data from IMPACTS used in this study are accessible through the
752 NASA Distributed Active Archive Center (McMurdie et al. 2019). Readers can find a complete
753 description of the McSnow model and its availability in Brdar and Seifert (2018).

754

755 **8. Author Contributions**

756 All authors contributed to the study design and methodology decisions. Andrew DeLaFrance
757 conducted the data curation and performed the simulations and computations from model output.
758 All authors contributed to the evaluation and interpretation of the results. Andrew DeLaFrance
759 prepared the manuscript with contributions from all co-authors.

760

761 **9. Competing Interests**

762 The authors declare that they have no conflict of interest.

763

764



765 **10. Acknowledgments**

766 The authors acknowledge the entire IMPACTS team for their excellence in the collection and
767 distribution of the robust IMPACTS dataset. The authors thank Axel Seifert and Christoph
768 Siewert for their support and feedback regarding application of the McSnow model. The authors
769 also expressly thank Aaron Bansemmer for processing of the microphysics probe data and helpful
770 discussions regarding its application and limitations. Funding was provided by NASA Future
771 Investigators in NASA Earth and Space Science Technology Grant # 80NSSC21K1589 and
772 NASA Grant # 80NSSC19K0338. NCAR provided resources for Andrew DeLaFrance to visit its
773 Mesoscale and Microscale Meteorology Laboratory (host Andrew Heymsfield), which benefited
774 the design and data curation for this analysis. Andrew Heymsfield is supported by the IMPACTS
775 field program and the National Science Foundation.

776

777

778 **11. References**

- 779 Bailey, M. P. and Hallett, J.: A Comprehensive Habit Diagram for Atmospheric Ice Crystals:
780 Confirmation from the Laboratory, AIRS II, and Other Field Studies, *J. Atmos. Sci.*, 66,
781 2888–2899, <https://doi.org/10.1175/2009JAS2883.1>, 2009.
- 782 Bansemmer, A., Delene D., Heymsfield A., O’Brien J., Poellot M., Sand K., Sova G., Moore J.,
783 and Nairy, C.: NCAR Particle Probes IMPACTS, Dataset available online from the
784 NASA Global Hydrometeorology Resource Center DAAC, Huntsville, Alabama, U.S.A.,
785 <https://doi.org/10.5067/IMPACTS/PROBES/DATA101>, 2022.
- 786 Bjerknes, J.: Extratropical Cyclones, in: *Compendium of Meteorology*, edited by: Malone, T. F.,
787 American Meteorological Society, Boston, MA, 577–598, https://doi.org/10.1007/978-1-940033-70-9_48, 1951.
- 789 Bohren, C. F. and Huffman, D. R.: *Absorption and Scattering of Light by Small Particles*, John
790 Wiley and Sons, New York, 530 pp., ISBN 3527618163, 1983.
- 791 Brdar, S. and Seifert, A.: McSnow: A Monte-Carlo Particle Model for Riming and Aggregation
792 of Ice Particles in a Multidimensional Microphysical Phase Space, *J. Adv. Model Earth
793 Sy.*, 10, 187–206, <https://doi.org/10.1002/2017MS001167>, 2018.
- 794 Bringi, V., Seifert, A., Wu, W., Thurai, M., Huang, G.-J., and Siewert, C.: Hurricane Dorian
795 Outer Rain Band Observations and 1D Particle Model Simulations: A Case Study,
796 *Atmosphere*, 11, 879, <https://doi.org/10.3390/atmos11080879>, 2020.
- 797 Brodzik, S.: Automated Surface Observing System (ASOS) IMPACTS, Dataset available online
798 from the NASA Global Hydrometeorology Resource Center DAAC, Huntsville,
799 Alabama, U.S.A., <https://doi.org/10.5067/IMPACTS/ASOS/DATA101>, 2022a.
- 800 Brodzik, S.: GOES IMPACTS, Dataset available online from the NASA Global
801 Hydrometeorology Resource Center DAAC, Huntsville, Alabama, U.S.A.,
802 <https://doi.org/10.5067/IMPACTS/GOES/DATA101>, 2022b.



- 803 Brown, P. R. A. and Francis, P. N.: Improved Measurements of the Ice Water Content in Cirrus
804 Using a Total-Water Probe, *J. Atmos. Oceanic Technol.*, 12, 410–414,
805 [https://doi.org/10.1175/1520-0426\(1995\)012<0410:IMOTIW>2.0.CO;2](https://doi.org/10.1175/1520-0426(1995)012<0410:IMOTIW>2.0.CO;2), 1995.
- 806 Chase, R. J., Nesbitt, S. W., and McFarquhar, G. M.: A Dual-Frequency Radar Retrieval of Two
807 Parameters of the Snowfall Particle Size Distribution Using a Neural Network, *J. Appl.*
808 *Meteorol. Clim.*, 60, 341–359, <https://doi.org/10.1175/JAMC-D-20-0177.1>, 2021.
- 809 Cholette, M., Milbrandt, J. A., Morrison, H., Paquin-Ricard, D., and Jacques, D.: Combining
810 Triple-Moment Ice with Prognostic Liquid Fraction in the P3 Microphysics Scheme:
811 Impacts on a Simulated Squall Line, *J. Adv. Model Earth Sy.*, 15, e2022MS003328,
812 <https://doi.org/10.1029/2022MS003328>, 2023.
- 813 Colle, B. A., Garvert, M. F., Wolfe, J. B., Mass, C. F., and Woods, C. P.: The 13–14 December
814 2001 IMPROVE-2 Event. Part III: Simulated Microphysical Budgets and Sensitivity
815 Studies, *J. Atmos. Sci.*, 62, 3535–3558, <https://doi.org/10.1175/JAS3552.1>, 2005.
- 816 Connolly, P. J., Emersic, C., and Field, P. R.: A Laboratory Investigation into the Aggregation
817 Efficiency of Small Ice Crystals, *Atmos. Chem. Phys.*, 12, 2055–2076,
818 <https://doi.org/10.5194/acp-12-2055-2012>, 2012.
- 819 DeLaFrance, A., McMurdie, L. A., Rowe, A. K., and Conrick, R.: Effects of Riming on Ice-
820 Phase Precipitation Growth and Transport Over an Orographic Barrier, *J. Adv. Model*
821 *Earth Sy.*, 16, e2023MS003778, <https://doi.org/10.1029/2023MS003778>, 2024.
- 822 Field, P. R., Hogan, R. J., Brown, P. R. A., Illingworth, A. J., Choulaton, T. W., and Cotton, R.
823 J.: Parametrization of Ice-Particle Size Distributions for Mid-Latitude Stratiform Cloud,
824 *Q. J. Roy. Meteor. Soc.*, 131, 1997–2017, <https://doi.org/10.1256/qj.04.134>, 2005.
- 825 Field, P. R., Heymsfield, A. J., and Bansemer, A.: Snow Size Distribution Parameterization for
826 Midlatitude and Tropical Ice Clouds, *J. Atmos. Sci.*, 64, 4346–4365,
827 <https://doi.org/10.1175/2007JAS2344.1>, 2007.
- 828 Grecu, M., Olson, W. S., Munchak, S. J., Ringerud, S., Liao, L., Haddad, Z., Kelley, B. L., and
829 McLaughlin, S. F.: The GPM Combined Algorithm, *J. Atmos. Ocean Tech.*, 33, 2225–
830 2245, <https://doi.org/10.1175/JTECH-D-16-0019.1>, 2016.
- 831 Hersbach, H., Bell, B., Berrisford, P., Hirahara, S., Horányi, A., Muñoz-Sabater, J., Nicolas, J.,
832 Peubey, C., Radu, R., Schepers, D., Simmons, A., Soci, C., Abdalla, S., Abellan, X.,
833 Balsamo, G., Bechtold, P., Biavati, G., Bidlot, J., Bonavita, M., De Chiara, G., Dahlgren,
834 P., Dee, D., Diamantakis, M., Dragani, R., Flemming, J., Forbes, R., Fuentes, M., Geer,
835 A., Haimberger, L., Healy, S., Hogan, R. J., Hólm, E., Janisková, M., Keeley, S.,
836 Laloyaux, P., Lopez, P., Lupu, C., Radnoti, G., De Rosnay, P., Rozum, I., Vamborg, F.,
837 Villaume, S., and Thépaut, J.: The ERA5 Global Reanalysis, *Q. J. Roy. Meteor. Soc.*,
838 146, 1999–2049, <https://doi.org/10.1002/qj.3803>, 2020.
- 839 Heymsfield, A. J.: A Comparative Study of the Rates of Development of Potential Graupel and
840 Hail Embryos in High Plains Storms, *J. Atmos. Sci.*, 39, 2867–2897,
841 [https://doi.org/10.1175/1520-0469\(1982\)039<2867:ACSOTR>2.0.CO;2](https://doi.org/10.1175/1520-0469(1982)039<2867:ACSOTR>2.0.CO;2), 1982.
- 842 Heymsfield, A. J., Bansemer, A., Schmitt, C., Twohy, C., and Poellot, M. R.: Effective Ice
843 Particle Densities Derived from Aircraft Data, *J. Atmos. Sci.*, 61, 982–1003,
844 [https://doi.org/10.1175/1520-0469\(2004\)061<0982:EIPDDF>2.0.CO;2](https://doi.org/10.1175/1520-0469(2004)061<0982:EIPDDF>2.0.CO;2), 2004.
- 845 Heymsfield, A., Bansemer, A., Heymsfield, G., Noone, D., Grecu, M., and Toohey, D.:
846 Relationship of Multiwavelength Radar Measurements to Ice Microphysics from the
847 IMPACTS Field Program, *J. Appl. Meteorol. Clim.*, 62, 289–315,
848 <https://doi.org/10.1175/JAMC-D-22-0057.1>, 2023.



- 849 Holton, J. R. and Hakim, G. J.: An Introduction to Dynamic Meteorology, 5th edition., Elsevier :
850 Academic Press, Amsterdam, 532 pp., ISBN 0123848679, 2012.
- 851 Iguchi, T., Seto, S., Meneghini, R., Yoshida, N., Awaka, J., Le, M., Chandrasekhar, V., Brodzik,
852 S., and Kubota, T.: GPM/DPR Level-2 Algorithm Theoretical Basis Document,
853 [https://www.eorc.jaxa.jp/GPM/doc/algorithm/ATBD_DPR_201811_with_Appendix3b.p](https://www.eorc.jaxa.jp/GPM/doc/algorithm/ATBD_DPR_201811_with_Appendix3b.pdf)
854 [df](https://www.eorc.jaxa.jp/GPM/doc/algorithm/ATBD_DPR_201811_with_Appendix3b.pdf), last access: May 2024, 2018.
- 855 Jensen, A. A. and Harrington, J. Y.: Modeling Ice Crystal Aspect Ratio Evolution during
856 Riming: A Single-Particle Growth Model, *J. Atmos. Sci.*, 72, 2569–2590,
857 <https://doi.org/10.1175/JAS-D-14-0297.1>, 2015.
- 858 Jensen, A. A., Harrington, J. Y., Morrison, H., and Milbrandt, J. A.: Predicting Ice Shape
859 Evolution in a Bulk Microphysics Model, *J. Atmos. Sci.*, 74, 2081–2104,
860 <https://doi.org/10.1175/JAS-D-16-0350.1>, 2017.
- 861 Kalesse, H., Szyrmer, W., Kneifel, S., Kollias, P., and Luke, E.: Fingerprints of a Riming Event
862 on Cloud Radar Doppler Spectra: Observations and Modeling, *Atmos. Chem. Phys.*, 16,
863 2997–3012, <https://doi.org/10.5194/acp-16-2997-2016>, 2016.
- 864 Kneifel, S., Kollias, P., Battaglia, A., Leinonen, J., Maahn, M., Kalesse, H., and Tridon, F.: First
865 Observations of Triple-Frequency Radar Doppler Spectra in Snowfall: Interpretation and
866 Applications, *Geophys. Res. Lett.*, 43, 2225–2233,
867 <https://doi.org/10.1002/2015GL067618>, 2016.
- 868 Lawson, R. P., Stewart, R. E., Strapp, J. W., and Isaac, G. A.: Aircraft Observations of the Origin
869 and Growth of Very Large Snowflakes, *Geophys. Res. Lett.*, 20, 53–56,
870 <https://doi.org/10.1029/92GL02917>, 1993.
- 871 Lawson, R. P., O’Connor, D., Zmarzly, P., Weaver, K., Baker, B., Mo, Q., and Jonsson, H.: The
872 2D-S (Stereo) Probe: Design and Preliminary Tests of a New Airborne, High-Speed,
873 High-Resolution Particle Imaging Probe, *J. Atmos. and Oceanic Tech.*, 23, 1462–1477,
874 <https://doi.org/10.1175/JTECH1927.1>, 2006.
- 875 Lawson, R. P., Gurganus, C., Woods, S., and Brientjes, R.: Aircraft Observations of Cumulus
876 Microphysics Ranging from the Tropics to Midlatitudes: Implications for a “New”
877 Secondary Ice Process, *J. Atmos. Sci.*, 74, 2899–2920, [https://doi.org/10.1175/JAS-D-17-](https://doi.org/10.1175/JAS-D-17-0033.1)
878 [0033.1](https://doi.org/10.1175/JAS-D-17-0033.1), 2017.
- 879 Leinonen, J.: High-level Interface to T-matrix Scattering Calculations: Architecture, Capabilities
880 and Limitations, *Opt. Express*, 22, 1655, <https://doi.org/10.1364/OE.22.001655>, 2014.
- 881 Leinonen, J. and Szyrmer, W.: Radar Signatures of Snowflake Riming: A Modeling Study, *Earth
882 Space Sci.*, 2, 346–358, <https://doi.org/10.1002/2015EA000102>, 2015.
- 883 Leinonen, J., Lebsock, M. D., Tanelli, S., Sy, O. O., Dolan, B., Chase, R. J., Finlon, J. A., Von
884 Lerber, A., and Moisseev, D.: Retrieval of Snowflake Microphysical Properties from
885 Multifrequency Radar Observations, *Atmos. Meas. Tech.*, 11, 5471–5488,
886 <https://doi.org/10.5194/amt-11-5471-2018>, 2018.
- 887 Li, L., Heymsfield, G., Carswell, J., Schaubert, D. H., McLinden, M. L., Creticos, J., Perrine, M.,
888 Coon, M., Cervantes, J. I., Vega, M., Guimond, S., Tian, L., and Emory, A.: The NASA
889 High-Altitude Imaging Wind and Rain Airborne Profiler, *IEEE T. Geosci. Remote*, 54,
890 298–310, <https://doi.org/10.1109/TGRS.2015.2456501>, 2016.
- 891 Lin, Y. and Colle, B. A.: A New Bulk Microphysical Scheme That Includes Riming Intensity
892 and Temperature-Dependent Ice Characteristics, *Mon. Weather Rev.*, 139, 1013–1035,
893 <https://doi.org/10.1175/2010MWR3293.1>, 2011.



- 894 Liu, G.: Approximation of Single Scattering Properties of Ice and Snow Particles for High
895 Microwave Frequencies, *J. Atmos. Sci.*, 61, 2441–2456, <https://doi.org/10.1175/1520->
896 0469(2004)061<2441:AOSSPO>2.0.CO;2, 2004.
- 897 Liu, G.: A Database of Microwave Single-Scattering Properties for Nonspherical Ice Particles,
898 *Bull. Amer. Meteor. Soc.*, 89, 1563–1570, <https://doi.org/10.1175/2008BAMS2486.1>,
899 2008.
- 900 Magono, C. and Lee, C. W.: Meteorological Classification of Natural Snow Crystals, *J. Fac. Sci.*,
901 Hokkaido University. Series 7, Geophysics, 2, 321–335, <http://hdl.handle.net/2115/8672>,
902 1966.
- 903 Mason, S. L., Chiu, C. J., Hogan, R. J., Moisseev, D., and Kneifel, S.: Retrievals of Riming and
904 Snow Density from Vertically Pointing Doppler Radars, *J. Geophys. Res.-Atmos.*, 123,
905 <https://doi.org/10.1029/2018JD028603>, 2018.
- 906 Mason, S. L., Hogan, R. J., Westbrook, C. D., Kneifel, S., Moisseev, D., and Von Terzi, L.: The
907 Importance of Particle Size Distribution and Internal Structure for Triple-Frequency
908 Radar Retrievals of the Morphology of Snow, *Atmos. Meas. Tech.*, 12, 4993–5018,
909 <https://doi.org/10.5194/amt-12-4993-2019>, 2019.
- 910 Matrosov, S. Y.: Modeling Backscatter Properties of Snowfall at Millimeter Wavelengths, *J.*
911 *Atmos. Sci.*, 64, 1727–1736, <https://doi.org/10.1175/JAS3904.1>, 2007.
- 912 McLinden, M., Li, L., and Heymsfield, G. M.: High Altitude Imaging Wind and Rain Airborne
913 Profiler (HIWRAP) IMPACTS, Dataset available online from the NASA Global
914 Hydrometeorology Resource Center DAAC, Huntsville, Alabama, U.S.A.,
915 <https://doi.org/10.5067/IMPACTS/HIWRAP/DATA101>, 2022a.
- 916 McLinden, M., Li, L., and Heymsfield, G. M.: Cloud Radar System (CRS) IMPACTS, Dataset
917 available online from the NASA Global Hydrometeorology Resource Center DAAC,
918 Huntsville, Alabama, U.S.A., <https://doi.org/10.5067/IMPACTS/CRS/DATA101>, 2022b.
- 919 McMurdie, L. A., Heymsfield, G., Yorks, J. E., and Braun, S. A.: Investigation of Microphysics
920 and Precipitation for Atlantic Coast-Threatening Snowstorms (IMPACTS) Collection.
921 Dataset available online from the NASA Global Hydrometeorology Resource Center
922 DAAC, Huntsville, Alabama, U.S.A., <https://doi.org/10.5067/IMPACTS/DATA101>,
923 2019.
- 924 McMurdie, L. A., Heymsfield, G. M., Yorks, J. E., Braun, S. A., Skofronick-Jackson, G.,
925 Rauber, R. M., Yuter, S., Colle, B., McFarquhar, G. M., Poellot, M., Novak, D. R., Lang,
926 T. J., Kroodsma, R., McLinden, M., Oue, M., Kollias, P., Kumjian, M. R., Greybush, S.
927 J., Heymsfield, A. J., Finlon, J. A., McDonald, V. L., and Nicholls, S.: Chasing
928 Snowstorms: The Investigation of Microphysics and Precipitation for Atlantic Coast-
929 Threatening Snowstorms (IMPACTS) Campaign, *B. Am. Meteorol. Soc.*, 103, E1243–
930 E1269, <https://doi.org/10.1175/BAMS-D-20-0246.1>, 2022.
- 931 Mishchenko, M. I., Travis, L. D., and Mackowski, D. W.: T-matrix Computations of Light
932 Scattering by Nonspherical Particles: A Review, *J. Quant. Spectrosc. Ra.*, 55, 535–575,
933 [https://doi.org/10.1016/0022-4073\(96\)00002-7](https://doi.org/10.1016/0022-4073(96)00002-7), 1996.
- 934 Mishchenko, M. I. and Travis, L. D.: Capabilities and Limitations of a Current FORTRAN
935 Implementation of the T-matrix Method for Randomly Oriented, Rotationally Symmetric
936 Scatterers, *J. Quant. Spectrosc. Ra.*, 60, 309–324, <https://doi.org/10.1016/S0022->
937 4073(98)00008-9, 1998.



- 938 Moisseev, D., Von Lerber, A., and Tiira, J.: Quantifying the Effect of Riming on Snowfall Using
939 Ground-Based Observations, *J. Geophys. Res.-Atmos.*, 122, 4019–4037,
940 <https://doi.org/10.1002/2016JD026272>, 2017.
- 941 Morrison, H. and Milbrandt, J.: Comparison of Two-Moment Bulk Microphysics Schemes in
942 Idealized Supercell Thunderstorm Simulations, *Mon. Wea. Rev.*, 139, 1103–1130,
943 <https://doi.org/10.1175/2010MWR3433.1>, 2011.
- 944 Morrison, H. and Milbrandt, J. A.: Parameterization of Cloud Microphysics Based on the
945 Prediction of Bulk Ice Particle Properties. Part I: Scheme Description and Idealized Tests,
946 *J. Atmos. Sci.*, 72, 287–311, <https://doi.org/10.1175/JAS-D-14-0065.1>, 2015.
- 947 Morrison, H., Curry, J. A., and Khvorostyanov, V. I.: A New Double-Moment Microphysics
948 Parameterization for Application in Cloud and Climate Models. Part I: Description, *J.*
949 *Atmos. Sci.*, 62, 1665–1677, <https://doi.org/10.1175/JAS3446.1>, 2005.
- 950 Morrison, H., Van Lier-Walqui, M., Fridlind, A. M., Grabowski, W. W., Harrington, J. Y.,
951 Hoose, C., Korolev, A., Kumjian, M. R., Milbrandt, J. A., Pawlowska, H., Posselt, D. J.,
952 Prat, O. P., Reimel, K. J., Shima, S., Van Dienenhoven, B., and Xue, L.: Confronting the
953 Challenge of Modeling Cloud and Precipitation Microphysics, *J. Adv. Model Earth Sy.*,
954 12, e2019MS001689, <https://doi.org/10.1029/2019MS001689>, 2020.
- 955 Novak, D. R., Bosart, L. F., Keyser, D., and Waldstreicher, J. S.: An Observational Study of
956 Cold Season–Banded Precipitation in Northeast U.S. Cyclones, *Weather Forecast.*, 19,
957 993–1010, <https://doi.org/10.1175/815.1>, 2004.
- 958 Oue, M., Kollias, P., Ryzhkov, A., and Luke, E. P.: Toward Exploring the Synergy Between
959 Cloud Radar Polarimetry and Doppler Spectral Analysis in Deep Cold Precipitating
960 Systems in the Arctic, *J. Geophys. Res.-Atmos.*, 123, 2797–2815,
961 <https://doi.org/10.1002/2017JD027717>, 2018.
- 962 Pruppacher, H. R. and Klett, J. D.: *Microphysics of Clouds and Precipitation*, 2nd rev. and enl.
963 ed., Kluwer Academic Publishers, Dordrecht ; Boston, 954 pp.,
964 <https://doi.org/10.1007/978-0-306-48100-0>, 1997.
- 965 Purcell, E. M. and Pennypacker, C. R.: Scattering and Absorption of Light by Nonspherical
966 Dielectric Grains, *Astrophys. J.*, 186, 705, <https://doi.org/10.1086/152538>, 1973.
- 967 Shima, S., Kusano, K., Kawano, A., Sugiyama, T., and Kawahara, S.: The Super-Droplet
968 Method for the Numerical Simulation of Clouds and Precipitation: A Particle-Based and
969 Probabilistic Microphysics Model Coupled with a Non-Hydrostatic Model, *Q. J. Roy.*
970 *Meteor. Soc.*, 135, 1307–1320, <https://doi.org/10.1002/qj.441>, 2009.
- 971 Skofronick-Jackson, G., Petersen, W. A., Berg, W., Kidd, C., Stocker, E. F., Kirschbaum, D. B.,
972 Kakar, R., Braun, S. A., Huffman, G. J., Iguchi, T., Kirstetter, P. E., Kummerow, C.,
973 Meneghini, R., Oki, R., Olson, W. S., Takayabu, Y. N., Furukawa, K., and Wilhelm, T.:
974 The Global Precipitation Measurement (GPM) Mission for Science and Society, *B. Am.*
975 *Meteorol. Soc.*, 98, 1679–1695, <https://doi.org/10.1175/BAMS-D-15-00306.1>, 2017.
- 976 Speirs, P., Gabella, M., and Berne, A.: A Comparison Between the GPM Dual-Frequency
977 Precipitation Radar and Ground-Based Radar Precipitation Rate Estimates in the Swiss
978 Alps and Plateau, *J. Hydrometeorol.*, 18, 1247–1269, <https://doi.org/10.1175/JHM-D-16-0085.1>, 2017.
- 980 Thornhill, K. L.: Turbulent Air Motion Measurement System (TAMMS) IMPACTS, Dataset
981 available online from the NASA Global Hydrometeorology Resource Center DAAC,
982 Huntsville, Alabama, U.S.A., <https://doi.org/10.5067/IMPACTS/TAMMS/DATA101>,
983 2022.



- 984 Thornhill, K. L., Anderson, B. E., Barrick, J. D. W., Bagwell, D. R., Friesen, R., and Lenschow,
985 D. H.: Air Motion Intercomparison Flights During Transport and Chemical Evolution in
986 the Pacific (TRACE-P)/ACE-ASIA, *J. Geophys. Res.-Atmos.*, 108, 2002JD003108,
987 <https://doi.org/10.1029/2002JD003108>, 2003.
- 988 Tridon, F., Battaglia, A., Chase, R. J., Turk, F. J., Leinonen, J., Kneifel, S., Mroz, K., Finlon, J.,
989 Bansemer, A., Tanelli, S., Heymsfield, A. J., and Nesbitt, S. W.: The Microphysics of
990 Stratiform Precipitation During OLYMPEX: Compatibility Between Triple-Frequency
991 Radar and Airborne In Situ Observations, *J. Geophys. Res.-Atmos.*, 124, 8764–8792,
992 <https://doi.org/10.1029/2018JD029858>, 2019.
- 993 Uccellini, L. W. and Kocin, P. J.: The Interaction of Jet Streak Circulations during Heavy Snow
994 Events along the East Coast of the United States, *Weather Forecast.*, 2, 289–308,
995 [https://doi.org/10.1175/1520-0434\(1987\)002<0289:TIOJSC>2.0.CO;2](https://doi.org/10.1175/1520-0434(1987)002<0289:TIOJSC>2.0.CO;2), 1987.
- 996 Van Weverberg, K., Vogelmann, A. M., Morrison, H., and Milbrandt, J. A.: Sensitivity of
997 Idealized Squall-Line Simulations to the Level of Complexity Used in Two-Moment
998 Bulk Microphysics Schemes, *Mon. Wea. Rev.*, 140, 1883–1907,
999 <https://doi.org/10.1175/MWR-D-11-00120.1>, 2012.
- 1000 Waldstreicher, J. and Brodzik, S.: NOAA Sounding IMPACTS, Dataset available online from
1001 the NASA Global Hydrometeorology Resource Center DAAC, Huntsville, Alabama,
1002 U.S.A., <https://doi.org/10.5067/IMPACTS/SOUNDING/DATA201>, 2022.
- 1003 Williams, C. R.: How Much Attenuation Extinguishes mm-Wave Vertically Pointing Radar
1004 Return Signals?, *Remote Sens.*, 14, 1305, <https://doi.org/10.3390/rs14061305>, 2022.
- 1005 Zhang, J., Howard, K., Langston, C., Vasiloff, S., Kaney, B., Arthur, A., Van Cooten, S.,
1006 Kelleher, K., Kitzmiller, D., Ding, F., Seo, D-J., Wells, E., and Dempsey C.: National
1007 Mosaic and Multi-Sensor QPE (NMQ) System: Description, Results, and Future Plans,
1008 *Bull. Amer. Meteor. Soc.*, 92, 1321- 1338, [https://doi.org/10.1175/2011BAMS-D-11-](https://doi.org/10.1175/2011BAMS-D-11-00047.1)
1009 [00047.1](https://doi.org/10.1175/2011BAMS-D-11-00047.1), 2011.